

Article

Influence of Particle Morphologies of LiFePO_4 on Water- and Solvent-Based Processing and Electrochemical Properties

Benjamin Starke ^{1,*}, Stefan Seidlmayer ², Sebastian Jankowsky ¹, Oleksandr Dolotko ²,
Ralph Gilles ² and Karl-Heinz Pettinger ¹

¹ Technology Center for Energy, University of Applied Sciences Landshut, Am Lurzenhof 1, 84036 Landshut, Germany; sebastian.jankowsky@haw-landshut.de (S.J.); karl-heinz.pettinger@haw-landshut.de (K.-H.P.)

² Heinz Maier-Leibnitz Zentrum (MLZ), Technische Universität München, 85748 Garching, Germany; Stefan.Seidlmayer@frm2.tum.de (S.S.); dolotko@ameslab.gov (O.D.); ralph.gilles@frm2.tum.de (R.G.)

* Correspondence: benjamin.starke@haw-landshut.de; Tel.: +49-8531-914044-41

Academic Editor: Derek J. McPhee

Received: 24 April 2017; Accepted: 19 May 2017; Published: 24 May 2017

Abstract: LiFePO_4 (LFP) primary particles and secondary agglomerates have been processed into water- and solvent-based cathodes. By means of neutron and X-ray diffraction it was found that no structural changes of LiFePO_4 occurred upon water- and solvent-based slurry preparation. Electrochemical characterization was carried out with full-cells and a distinct influence of particle morphology was observable. Water-based processing of primary particles leads to deficits in electrochemical performance while secondary agglomerates are non-sensitive to water during processing. In the presence of water, high mechanical stress during slurry preparation causes a partial detachment of carbon coating. However, this effect is negligible for secondary agglomerates since only surface particles are exposed to mechanical stress. Due to longer diffusion paths and the fact that secondary agglomerates represent a micro-heterogeneity in the cathode, the C-rate capability of secondary agglomerates is slightly lower than that of primary particles. This paper demonstrates that for any high energy application with moderate C-rates, secondary agglomerates hold a great potential for environmentally friendly and cost-efficient water-based cathode production.

Keywords: lithium-ion battery; LiFePO_4 ; ageing; water-based processing; sustainable battery manufacturing; morphology

1. Introduction

The growing energy revolution towards renewable power sources requires the decoupling of the availability of wind and solar energy and its demand, in order to grant stability to the grid [1]. One option for energy storage is lithium-ion batteries, due to their high coulombic efficiency and energy density [2,3]. These properties have already led to a widespread adoption of lithium-ion technology in mobile applications. However, there is also an increasing demand for lithium-ion batteries for stationary energy storage, for example, as home storage for self-generated photovoltaic energy [4].

The overall ecological balance of renewable energies is significantly dependent on the environmental sustainability of the associated energy storage technology. Despite the superior operational characteristics of lithium-ion batteries, their current manufacturing usually demands the use of toxic organic solvents such as *N*-methyl-2-pyrrolidone (NMP) [5,6]. During cathode drying, gaseous NMP has to be removed from the exhaust by costly and energy-intensive combustion or condensation. These facts severely influence the ecological balance. Replacing organic solvents with water would better facilitate battery production processes and maintain the favorable, environmentally-friendly nature of renewable energies [7].

When lithium-ion batteries are used for stationary energy storage in the commercial, and especially in the private sector, high levels of operational safety and reliability are essential. The battery safety depends, to a great extent, on the used cathode active material. A cathode material which meets these requirements is LiFePO_4 (LFP). It provides intrinsic safety [8–10], high tolerance towards abuse [11] and is furthermore, economically friendly. These characteristics make LiFePO_4 an appropriate material for sustainable battery production, in general, and for safety-oriented home storage applications, in particular.

However, despite the many advantages associated with LiFePO_4 it has a poor intrinsic electric conductivity of $10^{-9} \text{ S}\cdot\text{cm}^{-1}$ [12,13]. In order to overcome this disadvantage, the particle size of LiFePO_4 is reduced to the nano-scale which leads to a large specific surface and short diffusion length [8,14,15]. Further improvement of electrochemical performance is reached by standard carbon coating of LiFePO_4 particles.

The low bulk density which is correlated with nano-sized particles can be increased by the agglomeration of single nano-sized particles. The obtained secondary agglomerates combine the advantages of nano-sized particles and the higher bulk density of micro-sized ones. Higher bulk densities allow for producing cathodes with higher material- and energy-density and improved long-term cycling [16,17].

For a successful, economically-friendly water-based manufacturing process of LiFePO_4 cathodes, it is important that the active material is compatible with water as a solvent. LiFePO_4 and its behavior upon contact with moisture and water has been studied in recent years. It is reported that in direct contact with water, active lithium is lost by the formation of a surface layer consisting of Li_3PO_4 , which reduces the energy density of LiFePO_4 . This might also cause slight changes to lattice parameters which could be observable in diffraction experiments. However, this effect can be limited by reducing the period of water exposure [18]. It has also been found that carbon coating is not fully stable in water and partially detaches from the LiFePO_4 particle surface [19]. Notably, though, carbon coating has a protective function and prevents LiFePO_4 from accelerated ageing [20]. Studies have shown that LiFePO_4 cathodes can reach a good electrochemical performance after being processed in water [21]. The advantages of water-based elastomer binders in terms of cathode homogeneity and battery performance in comparison to solvent-based systems have also been recorded [22].

This article will evaluate the influence of the LiFePO_4 morphology on water-based processing, aspects of ageing, electrochemical characteristics and the suitability for environmentally-friendly battery production.

2. Experiment

A development-grade carbon coated LiFePO_4 (LFP) with two different morphologies was used for processing water- and organic-based cathodes. The first LiFePO_4 sample consisted of sub-micron single particles (referred to as PP) and the second sample consisted of PP agglomerated to spheres (referred to as SA).

The samples PP and SA were processed as water- and solvent-based slurries resulting in four different cathodes. The solvent which was used for the slurry preparation is indexed in the respective cathode identification, such as $\text{PP}_{\text{H}_2\text{O}}$. If no solvent is indicated (e.g., “PP” or “SA”), then the cathodes prepared with both solvents are meant.

For water-based slurries carboxymethyl cellulose (CMC MAC 200 HC, Sunrose, Nippon Paper Industries Co., Ltd., Tokyo, Japan) was dissolved in water and mixed with carbon black (Super C65, TIMCAL, Düsseldorf, Germany) and SBR (AY9391, ZEON, Tokyo, Japan) and PP or SA, respectively. All constituents were dispersed in a dissolver (DISPERMAT, VMA GETZMANN GmbH, Reichshof, Germany) for 30 min at 3000 rpm. The final solid content fractions were 88.6 wt % PP or SA, 6.0 wt % carbon black, 3.6 wt % SBR and 1.8 wt % CMC.

Slurries based on an organic solvent were obtained by dissolving PVDF (Solef 5130, Solvay) in *N*-methyl-2-pyrrolidone (NMP, Roth, Karlsruhe, Germany) and mixed with PP or SA and carbon

black. Dispersing the constituents was conducted as described for water-based slurries. The final solid content fractions were 88.0 wt % PP or SA, 6.0 wt % PVDF and 6.0 wt % carbon black.

After dissolution, the slurries were degassed in a planetary centrifugal mixer (THINKY, Laguna Hills, USA) for 4 min at 2200 rpm and then cast on a carbon-coated aluminum foil and dried under vacuum at 110 °C for at least 12 h.

The obtained cathodes were then assembled to full-cells by using an inorganic-filled PVDF separator and anodes composed of graphite (MAG-D, Hitachi Chemical Co., Ltd, Tokyo, Japan) (91.4 wt %), conductive carbon (Super C65, TIMCAL, Düsseldorf, Germany) (4.0 wt %), SBR (BM-400B, ZEON, Tokyo, Japan) (2.8 wt %) and CMC (MAC 200 HC, Sunrose, Nippon Paper Industries Co., Ltd., Tokyo, Japan) (1.8 wt %). For electrolyte, 1.5 mL of LP50 (1 M LiPF₆ in EC:EMC (1:1 wt %), BASF) was used. At least four full-cells were assembled of each cathode foil. The average areal capacity loading of the cathodes was 1.1 ± 0.1 mAh·cm⁻². The areal capacity balancing of anode: cathode was 0.9.

The full-cells were formed at room temperature with a charge rate of C/10 up to 3.65 V with a potential hold until the current dropped below C/20 and a discharge rate of C/10 to 2.0 V.

The subsequent C-rate test was carried out with a charge rate of C/10, C/5, C/2, 1 C, 2 C and 5 C by charging with the applied C-rate of up to 3.65 V with a potential hold until the current dropped below C/20 and discharged with the corresponding C-rate to 2.0 V. Each C-rate charge and discharge was repeated three times. For each full-cell, the different C-rate currents were calculated on the basis of the discharge capacity of the second cycle. The long-term capacity fading of full-cells was examined by charging at 1 C to 3.65 V with a potential hold until the current dropped below C/20 and discharged to 2.0 V at 1 C for 500 cycles.

A field emission scanning electron microscope (FE-SEM) (Merlin Compact, Zeiss, Oberkochen, Germany) was used to take micrographs of the prepared cathodes.

The lattice parameters of the pristine PP were analyzed by using neutron powder diffraction analysis. Elastic coherent neutron scattering experiments were performed on the high-resolution powder diffractometer SPODI at the neutron source FRM II at the Heinz Maier-Leibnitz Zentrum (Garching, Germany) [23]. Monochromatic neutrons ($\lambda = 1.5482$ Å) were obtained at a 155° take-off angle using the (551) reflection of a vertically-focused composite Ge monochromator. A vertical position-sensitive multidetector (300 mm effective height) consisting of 80 ³He tubes and covering a 2 θ angular range of 160 deg. was used for data collection. Measurements were performed in Debye-Scherrer geometry. The powder sample (ca. 2 cm³) was placed into a vanadium can 13 mm in diameter with a wall as thin as 0.15 mm. For minimization of the preferred orientation effect on the diffraction pattern, the sample was constantly rotated during data collection.

Additionally, the crystal structures of PP and SA in the prepared cathodes were studied by means of X-ray diffraction (XRD) (Empyrean, PANalytical, Almelo, Netherlands) using transmission geometry and Mo-K _{α 1/ α 2} radiation ($\lambda = 0.70932$ Å, U = 55 kV, I = 40 mA, ratio K _{α 1}/K _{α 2} \approx 0.30–0.33) and a step size of 0.008° (2 θ). Beam divergence was limited to 0.02° with Soller Slits and a 0.25° divergence slit. All data analysis was performed by RIETVELD refinements using the Highscore software package [24]. RIETVELD refinements were carried out using THOMPSON-COX-HASTINGS pseudo-VOIGT function [25] and FINGER-COX-JEPHCOAT profile asymmetry treatment to fit the data [26]. The aluminium current collector phase was treated with a PAWLEY-Fit [27].

3. Results and Discussion

To analyze and compare the influence of water- and NMP-based slurry preparation on the structural properties of LFP, X-ray diffraction was applied. In order to quantify the influence of both applied solvents, additional lattice parameters of a pristine PP powder sample were determined via high-resolution neutron diffraction. It was only carried out for pristine PP material in order to verify the lithium content of the pristine samples, due to the better contrast of neutrons for lithium compared to XRD. For comparison, the neutron and X-ray diffraction data in Figure 1 are plotted vs. d-spacing.

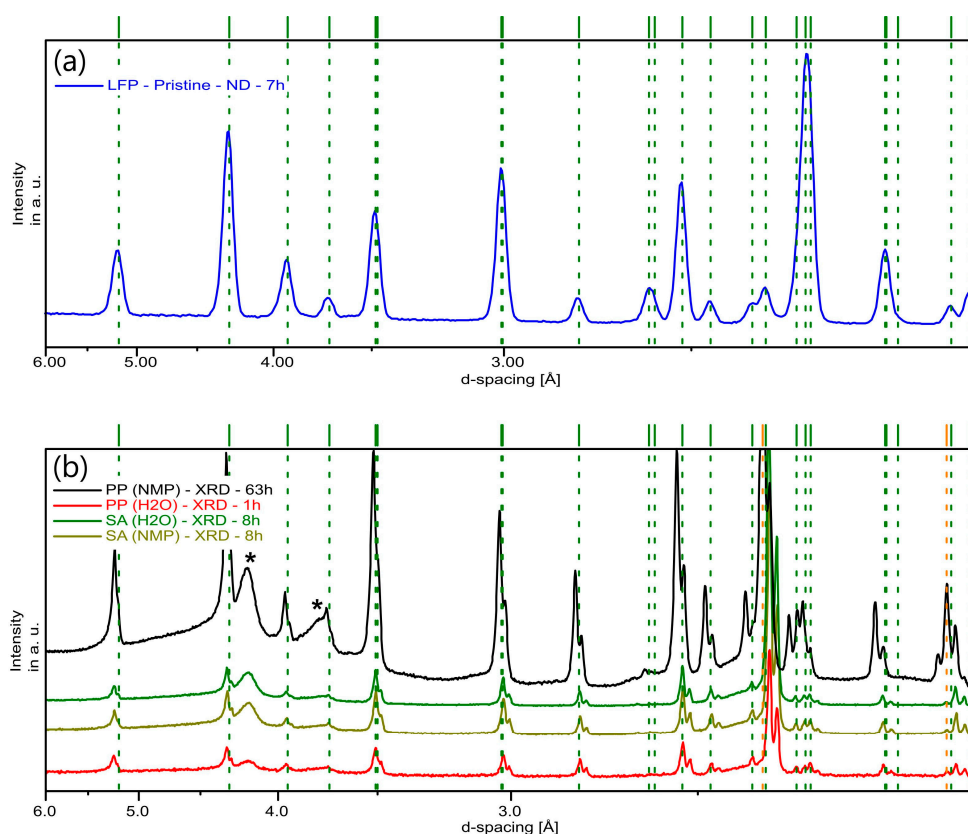


Figure 1. Comparison of the X-ray and neutron diffraction patterns of studied LiFePO_4 (LFP) samples: (a) Neutron diffraction data of pristine LFP-powder ($\lambda = 1.5482 \text{ \AA}$); (b) X-ray diffraction patterns of prepared cathodes ($\lambda = 0.70932 \text{ \AA}$). Data are plotted versus d-spacing for better comparison of the different wavelength data. For the visualization, no further data treatment has been performed. Thus, the visible shifts of the XRD patterns are due to different sample offset values. Sample offset was refined as a parameter in the RIETVELD refinements and thus had no impact on the lattice parameter estimation. Asterisks * mark background peaks from the polymer of the protective bag holding the cathodes. Green and orange lines mark LiFePO_4 reflections and Al current collector reflections, respectively. Diffraction patterns are arbitrarily offset in y -axis for better visibility.

For the neutron data, 7 h acquisition time was used and a comparable 8 h time was used for the first two XRD measurements of cathodes. A variation of time (1 h and 63 h) also proved that sufficient data quality is already obtained after 1 h and the 63 h data set shows that no additional reflections have been overlooked. Different peak intensities for identical reflections in the neutron and XRD plots are due to the different scattering cross section of the two methods. Also, the additional $K_{\alpha 2}$ -reflection is visible in the XRD plots as a shoulder right to the $K_{\alpha 1}$ -peak. The results of the structural studies and lattice parameters from the RIETVELD refinement of the LFP-phase are given in Table 1.

The results of X-ray and neutron diffraction show that neither water nor NMP have any significant influence on the structure of PP and SA in terms of slurry preparation and cathode coating. The highest deviation with a value of 0.0017 \AA between the pristine and processed PP can be found for parameter a when it is processed in water (PP_{NMP}). For SA the largest difference is observed for the lattice parameter c with a value of 0.0014 \AA after water-based processing ($\text{SA}_{\text{H}_2\text{O}}$). However, it has to be taken into account that deviations in the range of $\approx 0.001 \text{ \AA}$ have to be interpreted carefully since they are in the range of measurement inaccuracy [28–31]. This applies in particular in the present case, as no systematic tendency in the change of lattice parameters can be observed and negligible variations seem to be random. Thus, we regard the active material as such to be non-sensitive to water and stable during slurry preparation.

Table 1. Structural data from RIETVELD refinements of structure models based on X-ray diffraction (XRD) and neutron diffraction (ND) for a pristine PP sample and PP_{H_2O} , PP_{NMP} , SA_{H_2O} and SA_{NMP} cathodes ($P n m a$ Space group). Numbers in parentheses give statistical deviations in the last significant digits.

Sample		Pristine PP	PP_{H_2O}	PP_{NMP}	SA_{H_2O}	SA_{NMP}
Measurement method		ND	XRD	XRD	XRD	XRD
Lattice parameter/Å	<i>a</i>	10.3280(1)	10.3275(2)	10.3263(1)	10.3266(2)	10.3269(1)
	<i>b</i>	6.0063(1)	6.0055(1)	6.0053(1)	6.0054(3)	6.0058(1)
	<i>c</i>	4.6911(1)	4.6906(1)	4.6901(1)	4.6914(1)	4.6916(1)

The visual appearance and quality of the prepared cathodes was evaluated via FE-SEM and the obtained micrographs are shown in Figure 2.

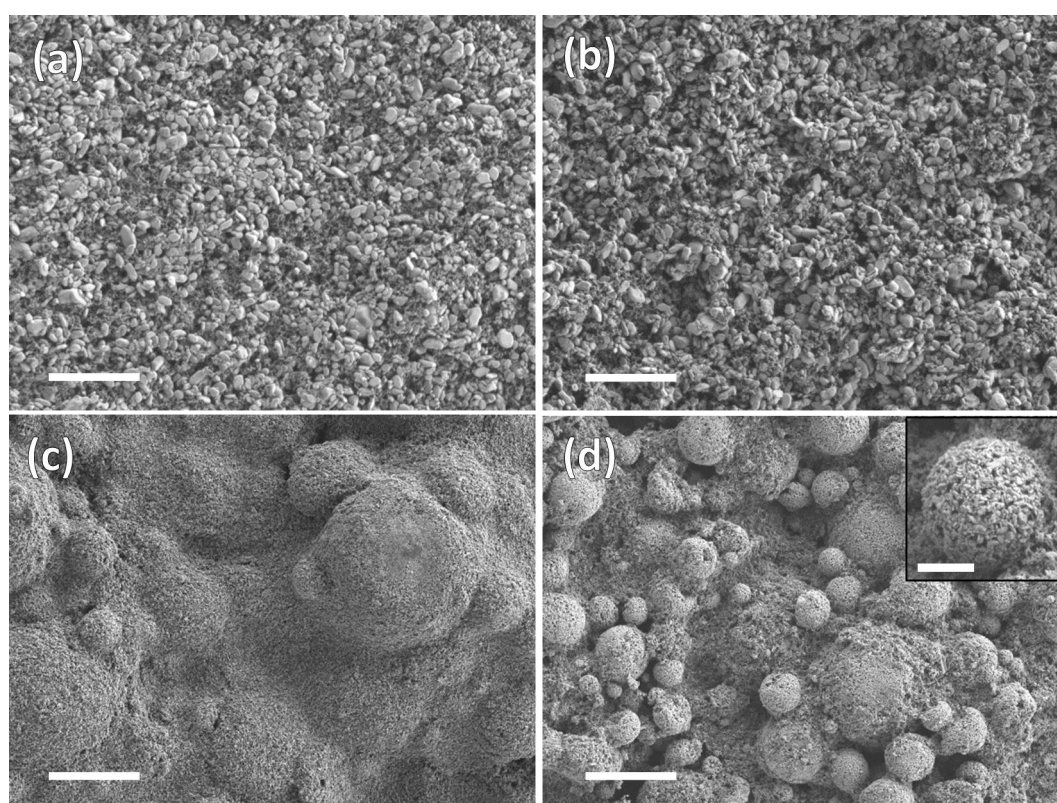


Figure 2. FE-SEM micrographs of the prepared cathodes: (a) PP_{H_2O} cathode (scale bar: 4 μm); (b) PP_{NMP} cathode (scale bar: 4 μm); (c) SA_{H_2O} cathode (scale bar: 20 μm); (d) SA_{NMP} cathode (scale bar: 20 μm); inset in (d) shows a secondary agglomerate without conductive carbon covering (scale bar: 3 μm). Micrographs were recorded at a voltage of 1.0 kV and a working distance of 5 mm.

As seen in Figure 2a,b, the constituents of the PP_{H_2O} and PP_{NMP} cathodes show an optimum, homogeneous distribution.

Figure 2c,d shows the structure of the SA_{H_2O} and SA_{NMP} cathodes. The secondary agglomerates of the SA_{H_2O} cathode in Figure 2c are homogeneously covered with a thin layer of binder and incorporated conductive carbon and primary particles of LFP. The shape of the underlying secondary agglomerates is, however, visible. The primary particles on the cathode surface are not necessarily detached from the secondary agglomerates as a result of mechanic stress during slurry preparation. They might also represent a small fraction of residual particles which were not bound in secondary agglomerates during the agglomerating process. The SA_{NMP} cathode in Figure 2d has a different

appearance in comparison to the SA_{H2O} cathode. The constituents are distributed homogeneously, but some secondary agglomerates on the surface are only partially covered with conductive carbon. This can be caused by a longer period of drying of NMP-based cathodes after the coating step due to the higher boiling point of NMP. In the wet state, the slurry constituents are still movable and might separate to a certain extent depending on the period of drying. Parameters such as solid and solvent content in the slurry, electrode thickness, coating speed or the electrode drying procedure were not varied during the cathode preparation and are therefore assumed to have no influence on different cathode appearances.

After the formation step the C-rate performance test was carried out for full-cells prepared with all four different cathodes. The obtained discharge curves are shown in Figure 3. The highest observed specific discharge capacity (at C/10) was set to 100% for each full-cell and all other observed discharge capacities were set in relative relation to this value. In consideration of the initial capacity loss caused by the formation of the SEI layer, the areal capacities (at C/10) of PP_{H2O}, PP_{NMP}, SA_{H2O} and SA_{NMP} were 0.98, 0.98, 0.92 and 0.94 mAh·cm⁻², respectively.

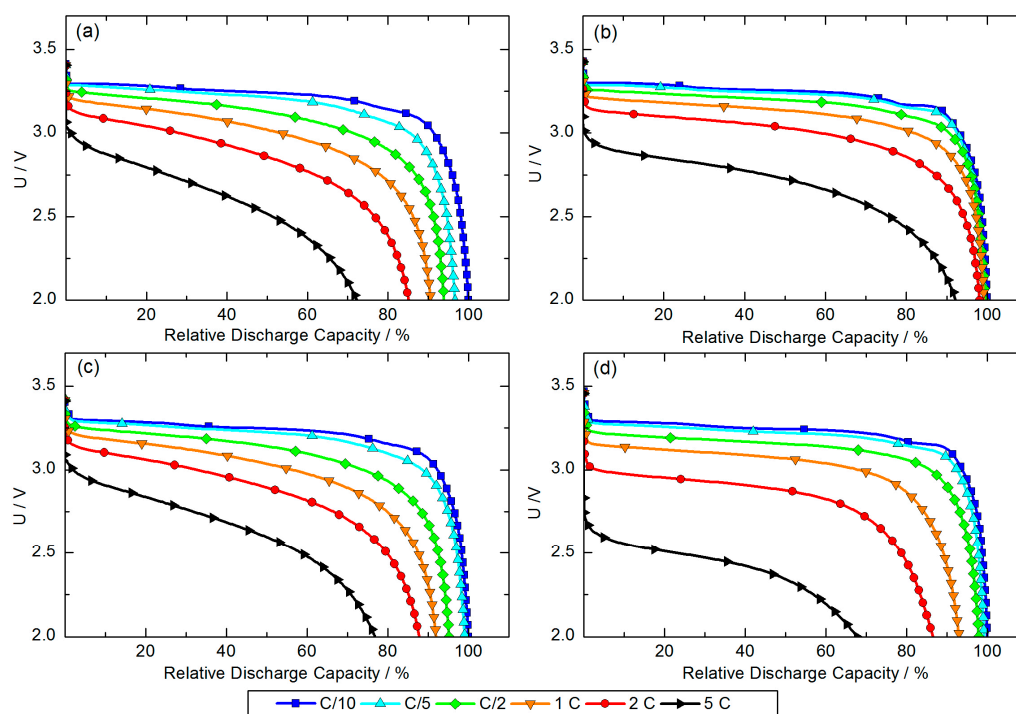


Figure 3. C-rate test of full-cells assembled with differently processed PP and SA cathodes: (a) PP_{H2O}; (b) PP_{NMP}; (c) SA_{H2O}; (d) SA_{NMP}.

Comparing the discharge curves of full-cells assembled with PP_{H2O} and PP_{NMP} cathodes (Figure 3a,b) shows a distinct difference in C-rate capability. The discharge capacity of the full-cell assembled with a PP_{H2O} cathode decreases constantly with an increased C-rate, but still reaches a reasonable 72% of the discharge capacity observed at C/10. In contrast full-cells assembled with PP_{NMP} cathodes show more or less no decrease of discharge capacity for C-rates up to 2 C. At a 5 C-rate, full-cells still reach 92% relative discharge capacity, which demonstrates a very good C-rate capability. The difference between PP_{H2O} and PP_{NMP} cathodes cannot be explained by the cathode structure observed via FE-SEM because for both solvents, a homogeneous distribution of constituents was confirmed.

The discharge curves of full-cells assembled with SA_{H2O} and SA_{NMP} cathodes (Figure 3c,d) appear similar for C-rates from C/10–1 C. For both full-cells, approximately 92% of the discharge capacity observed at C/10 is reached when cells are discharged at a 1 C-rate. Differences in discharge behavior

become significant at a 2 C-rate. Both full-cells reach almost the same relative discharge capacity (88% for the SA_{H2O}-based full-cell, 87% for the SA_{NMP}-based full-cell), but the initial voltage drops (IR-drop) at the beginning of discharge differ. The voltage of the full-cell assembled with a SA_{H2O} cathode drops down to approximately 3.2 V while it drops down to approximately 3.0 V in the case of the full-cell assembled with a SA_{NMP} cathode. This difference in IR-drop and relative discharge capacity becomes more distinct at a 5 C-rate. The reason for the lower internal resistance of the full-cell assembled with a SA_{H2O} cathode is very likely the better distribution of cathode constituents as it was observed via FE-SEM.

In the case of full-cells assembled with PP_{H2O} or PP_{NMP} cathodes, we do not see such a difference in IR-drop at higher C-rates, but the voltage-curve of the full-cell assembled with a PP_{NMP} cathode drops slower over the discharge process.

An explanation for the different discharge characteristics of PP_{NMP} cathodes and both SA_{H2O} and SA_{NMP} cathodes, is the morphology. Each secondary agglomerate of SA itself represents a small-scale heterogeneity of the cathode coating, but for an optimum battery performance a highest possible homogeneity of electrode constituents is striven. This can be realized by using PP which leads to a higher C-rate capability. Longer diffusion paths to the inner particles of SA can be seen as a further reason for lower C-rate capability.

The different C-rate capability of PP_{H2O}- and PP_{NMP}-based full-cells can be caused by partial detachment of carbon coating caused by water-based processing, thereby resulting in a higher internal resistance and lower discharge capacity at increased C-rates. An influence of the areal capacity of the cathodes is unlikely since it varies only in a narrow range of 0.06 mAh·cm⁻² and thus might not significantly influence the C-rate performance of each battery.

A difference in internal resistance was also found in the charge behavior of PP- and SA-based full-cells. Figure 4 shows that in full-cells assembled with the SA_{H2O}, SA_{NMP} and PP_{NMP} cathodes, the transfer of the charge was 93.4–94.3% during the constant current phase (CC-phase) and the residual charge occurred during the constant voltage phase (CV-phase). Thus, these full-cells show nearly the same charge characteristics. In contrast, full-cells assembled with PP_{H2O} cathodes transferred 74.1% and 25.9% during the CC- and CV-phase, respectively.

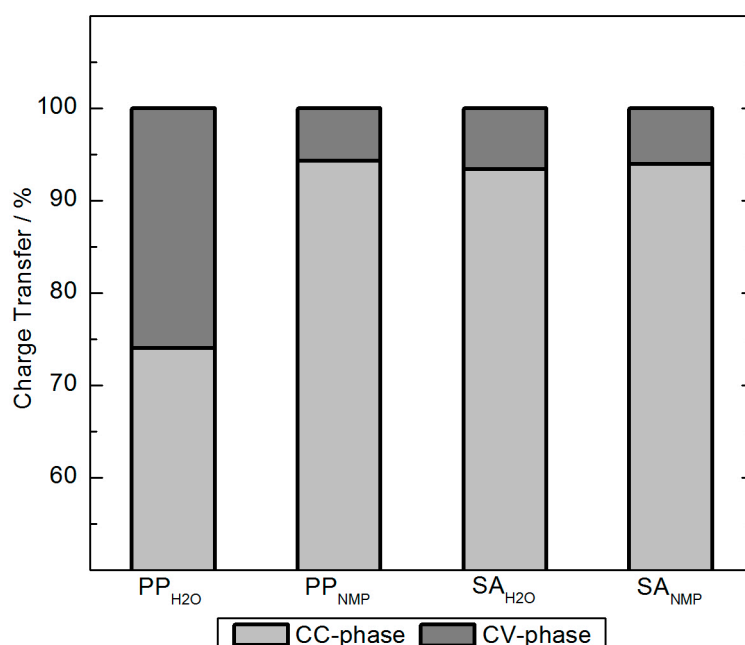


Figure 4. Charge transfer during constant current (CC) and constant voltage CV) phase in full-cells assembled with all four different cathodes. The applied charge rate was C/2.

An explanation, therefore, is that the upper cutoff voltage of 3.65 V is reached faster due to higher internal resistance in the full-cell assembled with the PP_{H_2O} cathode and thus, more charge has to be transferred at a constantly decreasing current during the CV-phase. For SA, no influence of the slurry solvent on the charge behavior was observed.

Figure 5 shows the result of the long-term cycling at a 1 C-rate. The highest specific discharge capacity was reached by full-cells assembled with PP_{NMP} cathodes (set to 100% in Figure 5). SA-based full-cells reach 96% relative discharge capacity independently from the solvent used for slurry preparation and their curves are more or less completely overlapped. Full-cells assembled with PP_{H_2O} cathodes reach only 86% relative discharge capacity. This direct comparison of relative discharge capacities shows the strong morphologic influence on the performance of the battery. Slight deviations between the observed capacities at a 1 C-rate in Figures 3 and 5 were caused by the fact that for the C-rate test, each battery was individually normalized to 100%, while values for the long-term cycling were obtained by average values of at least four batteries per parameter set and normalization of all average values to the highest observed discharge capacity.

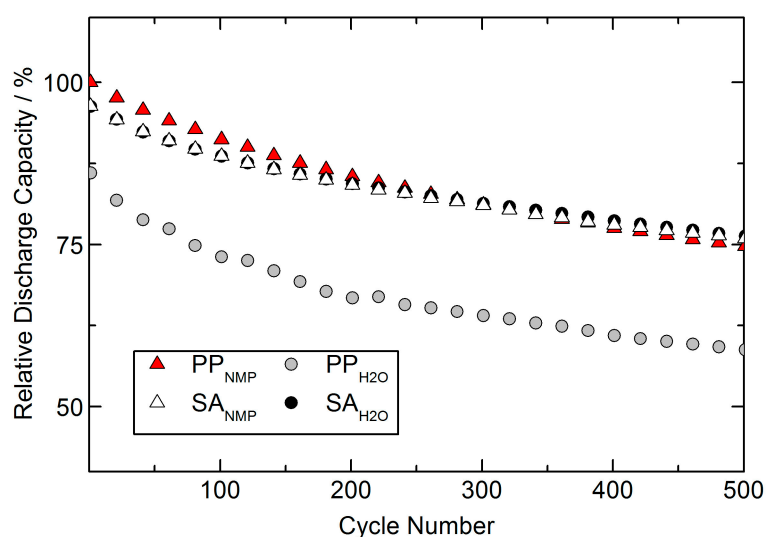


Figure 5. Capacity retention with increasing cycle numbers of the different full-cells. The highest observed specific discharge capacity (average of PP_{NMP} -based full-cells) has been set to 100%. All other specific discharge capacities are set in relative relation to this value. Values represent the average of at least four full-cells per parameter set.

The capacity fading rate of PP-based full-cells is slightly higher. In particular, full-cells assembled with PP_{H_2O} cathodes fade stronger during the first 100 cycles. This is a further indicator for partial detachment of carbon coating caused by water-based slurry preparation. Assuming traces of moisture contamination in the electrolyte, hydrofluoric acid is formed during cycling which can corrode the uncoated surface of PP and dissolve iron atoms from the structure. This causes an increased capacity fading. Complete and intact carbon coating effectively protects the PP surface from corrosion [20]. Since the difference in fading is less pronounced, we assume only minor detachment of the carbon coating caused by water-based processing.

The lower fading rate of SA-based full-cells leads to a crossing of the capacity curves of PP_{NMP} -based full-cells and SA-based full-cells after approximately 300 cycles. Thus, even if full-cells assembled with PP_{NMP} cathodes show the highest initial discharge capacity, SA-based full-cells feature a better long-term cycling behavior, which comes into effect after 300 cycles.

Additionally, the coulomb efficiency was evaluated for the full-cells of long-term cycling. The coulomb efficiency was calculated as the ratio of $Q_{Discharge}/Q_{Charge}$. The coulomb efficiency

is illustrated in Figure 6. The values of each parameter represent the average of the same full-cells used for the long-term cycling.

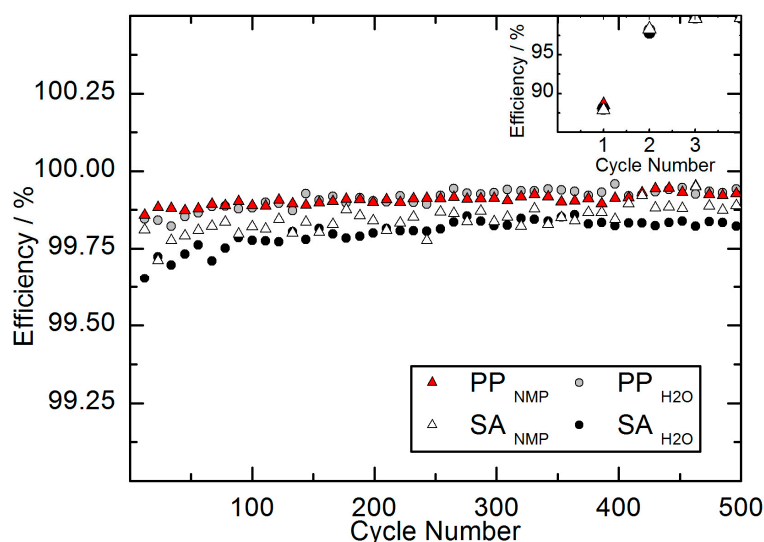


Figure 6. Coulomb efficiency obtained from full-cells of the long term cycling (500 cycles) at a 1 C-rate. Inset illustrates the reduced coulomb efficiency during the first three cycles caused by the irreversible capacity loss (ICL) during the initial formation of the SEI layer.

As seen in the inset of Figure 6, the coulomb efficiency is reduced in the first cycle. This is caused by the lithium consuming formation of the protective SEI layer on the anodic graphite. The formation of the SEI layer corresponds with a significant irreversible capacity loss (ICL) mainly during the first and second cycle. The observed capacity losses after the formation step were $11.5 \pm 0.6\%$, $11.9 \pm 0.9\%$, $12.1 \pm 0.8\%$ and $12.0 \pm 0.4\%$ for PP_{NMP}, PP_{H2O}, SA_{NMP} and SA_{H2O}, respectively. Since the SEI formation mainly takes place during the first cycle, the capacity losses were moderate after the second cycle. Ongoing SEI formation during the second cycle caused capacity losses of $1.7 \pm 0.2\%$, $1.8 \pm 0.3\%$, $1.7 \pm 0.2\%$ and $2.2 \pm 0.2\%$ for PP_{NMP}, PP_{H2O}, SA_{NMP} and SA_{H2O}, respectively. The capacity losses during the first two cycles varied only in a narrow range for the different parameter sets and are in good correlation with the analyzed coulomb efficiencies during the first cycles. Figure 6 also reveals that all full-cells have a reasonable coulomb efficiency above 99.5% during the long-term cycling. A slight, constant increase of coulomb efficiency corresponds with a decreasing capacity fading as shown in Figure 5. Stronger fading should usually result in lower coulomb efficiency because parasitic processes continue during formation of the new SEI layer. Remarkably, in comparison with the long-term fading we observe a reversed order of coulomb efficiency for the different parameter sets. SA-based full-cells show the lower capacity fading over 500 cycles, but also exhibit the lower coulomb efficiency. In contrast, PP-based full-cells reveal the higher coulomb efficiency but demonstrate stronger fading. One explanation might be the different morphology. Studies have shown that the particle size distribution of active material influences the relation between coulombic efficiency and capacity fading [32]. A difference in particle size distribution can cause a lower fading and simultaneously lower coulomb efficiency. Since the LFP primary particles analyzed in this study are the same material used for the preparation of secondary agglomerates, the particle size distribution is identical in terms of the particles. But an influence might be caused by an additional particle size distribution obtained by the secondary structure of agglomerates. Additionally, the discussion of coulomb efficiency in the context of capacity fading and battery quality should generally be handled with care. Other factors, such as diffusion-induced stress (DIS) and the capacity ratio of anode:cathode also play a significant role [33]. Just how far the morphology of the same active material stands in correlation to coulomb efficiency and long-term capacity evolution will be the subject of further, detailed studies.

Taking into account the results of the charge and discharge behaviour and long-term cycling, we come to the following explanation of the differences:

The process time, from the immersion of active material into water to the dried cathodes, was short enough to prevent structural changes of the active material itself. However, during slurry dissolution the active material particles are exposed to high mechanical stress and shear rates. In the case of PP additional contact to water causes a partial detachment of carbon coating. But if primary particles (PP) are agglomerated to spheres (SA) the major fraction of particles is located inside the agglomerates and protected from mechanical stress. The concurrent exposure to water and mechanical stress only takes place on particles at the outer layer of agglomerates and thus a partial detachment of carbon coating can only occur on the surface particles. This effect is negligible since no difference in performance was found at moderate C-rates. Differences occurring at higher C-rates were rather caused by using different binders, and the water-based CMC binder resulted in a favorable performance. The fact that cathodes containing SA did not reach the C-rate performance of PP_{NMP} cathodes is assumed to be caused by longer diffusion paths in the case of SA and a higher cathode homogeneity, which was reached by using PP.

4. Conclusions

Structural analyses have shown that PP and SA are, as such, not affected by water-based processing.

The electrochemical characteristics of PP and SA processed to water- and NMP-based cathodes have been evaluated in full-cells and the distinct morphologic influence has been stated.

If LFP is planned to be used for high power applications demanding fast charge and discharge rates, PP should be used and processed in the standard organic solvent procedure.

Based on our data, we give a clear recommendation for water-based processing in any cases where moderate C-rates are sufficient and high energy density is desired. For water-based processing, the superior SA should be used since these even performed better at elevated C-rates in comparison to the NMP-based process. Thus, SA has a high potential to combine environmentally-friendly battery production with very high operational safety. Another advantage is the slightly better long-term cycling behavior, which is of special interest to those developing applications with a desired long life-time and high capital expenditure, such as home energy storage. It is expected that breaking up secondary agglomerates by calendaring SA cathodes can possibly shift the C-rate performance towards values observed for PP_{NMP} cathodes.

Supplementary Materials: The following are available online at www.mdpi.com/2071-1050/9/6/888/s1, List of refined parameter values of X-ray and neutron diffraction: Table S1: LFP Phase literature parameters, Li occupancy was set to 1 prior to starting the refinements. Data obtained by neutron powder diffraction [30], ICSD #-155816, Table S2: Al Phase starting parameters. Data obtained by XRD [28], ICSD #-43423, Table S3: Refined parameters of the LFP phase and R-values of the Rietveld refinements Standard uncertainty values are given in parentheses as refined by Highscore without multiplying the values with the R_{wp} -value of the fit. ${}^1K\alpha_2/K\alpha_1$ ratios were determined by refinement using a Si-powder standard (NIST 640d), Table S4: Refined Al phase Pawley fit parameters.

Acknowledgments: The authors acknowledge the German Research Foundation (Deutsche Forschungsgemeinschaft, DFG) for sponsoring the FE-SEM (Merlin Compact, Zeiss). We also like to thank the Heinz Maier-Leibnitz Zentrum (MLZ) for granting us beam time at the neutron source and use of the Materials Science laboratory. This work was supported by the Bavarian Ministry of Education and Culture (grant number: VIII.2-F1116.LA/13/3). One of the authors (S. Seidlmayer) thanks the Bavarian Ministry of Economic Affairs and Media, Energy and Technology under the auspices of the EEBatt project.

Author Contributions: Benjamin Starke conceived, designed and performed the electrochemical experiments, analyzed the electrochemical data and drafted the manuscript. Stefan Seidlmayer performed and analyzed XRD measurements, analyzed the data of neutron diffraction and helped to draft the manuscript. Sebastian Jankowsky supported CE analysis and interpretation and helped to draft the manuscript. Oleksandr Dolotko performed neutron diffraction measurements and helped to draft the manuscript. Ralph Gilles helped to analyze X-ray and neutron diffraction and to draft the manuscript. Karl-Heinz Pettinger helped to analyze electrochemical data and to draft the manuscript.

Conflicts of Interest: The authors declare no conflict of interest.

References

1. Dunn, B.; Kamath, H.; Tarascon, J.M. Electrical energy storage for the grid: A battery of choices. *Science* **2011**, *334*, 928–935. [[CrossRef](#)] [[PubMed](#)]
2. Goodenough, J.B.; Park, K.S. The Li-ion rechargeable battery: A perspective. *J. Am. Chem. Soc.* **2013**, *135*, 1167–1176. [[CrossRef](#)] [[PubMed](#)]
3. Xu, T.; Wang, W.; Gordin, M.L.; Wang, D.; Choi, D. Lithium-ion batteries for stationary energy storage. *JOM* **2010**, *62*, 24–30. [[CrossRef](#)]
4. Naumann, M.; Karl, R.C.; Truong, C.N.; Jossen, A.; Hesse, H.C. Lithium-ion battery cost analysis in PV-household application. *Energy Procedia* **2015**, *73*, 37–47. [[CrossRef](#)]
5. Pohjalainen, E.; Räsänen, S.; Jokinen, M.; Yliniemi, K.; Worsley, D.A.; Kuusivaara, J.; Juurikivi, J.; Ekqvist, R.; Kallio, T.; Karppinen, M. Water soluble binder for fabrication of Li₄Ti₅O₁₂ electrodes. *J. Power Sources* **2013**, *226*, 134–139. [[CrossRef](#)]
6. Carnerup, M.A.; Saillenfait, A.M.; Jönsson, B.A.G. Concentrations of N-methyl-2-pyrrolidone (NMP) and its metabolites in plasma and urine following oral administration of NMP to rats. *Food Chem. Toxicol.* **2005**, *43*, 1441–1447. [[CrossRef](#)] [[PubMed](#)]
7. Daniel, C. Lithium Ion Batteries and Their Manufacturing Challenges. In *The Bridge*; Latanision, R.M., Fletcher, C.H., Eds.; National Academy of Engineering: Washington, DC, USA, 2015; Volume 45, pp. 21–24.
8. Yamada, A.; Chung, S.C.; Hinokuma, K. Optimized LiFePO₄ for lithium battery cathodes. *J. Electrochem. Soc.* **2001**, *148*, A224–A229. [[CrossRef](#)]
9. Benoit, C.; Franger, S. Chemistry and electrochemistry of lithium iron phosphate. *J. Solid State Electrochem.* **2008**, *12*, 987–993. [[CrossRef](#)]
10. Arnold, G.; Garche, J.; Hemmer, R.; Ströbele, S.; Vogler, C.; Wohlfahrt-Mehrens, M. Fine-particle lithium iron phosphate LiFePO₄ synthesized by a new low-cost aqueous precipitation technique. *J. Power Sources* **2003**, *119–121*, 247–251. [[CrossRef](#)]
11. Larsson, F.; Mellander, B.E. Abuse by external heating, overcharge and short circuiting of commercial lithium-ion battery cells. *J. Electrochem. Soc.* **2014**, *161*, A1611–A1617. [[CrossRef](#)]
12. Padhi, A.K. Phospho-olivines as positive-electrode materials for rechargeable lithium batteries. *J. Electrochem. Soc.* **1997**, *144*, 1188. [[CrossRef](#)]
13. Malik, R.; Burch, D.; Bazant, M.; Ceder, G. Particle size dependence of the ionic diffusivity. *Nano Lett.* **2010**, *10*, 4123–4127. [[CrossRef](#)] [[PubMed](#)]
14. Satyavani, T.; Ramya, K.B.; Rajesh, K.V.; Srinivas, K.A.; Naidu, S.V. Effect of particle size on dc conductivity, activation energy and diffusion coefficient of lithium iron phosphate in Li-ion cells. *Eng. Sci. Technol. Int. J.* **2016**, *19*, 40–44. [[CrossRef](#)]
15. Julien, C.M.; Mauger, A.; Zaghbi, K. Surface effects on electrochemical properties of nano-sized LiFePO₄. *J. Mater. Chem.* **2011**, *21*, 9955. [[CrossRef](#)]
16. Wu, N.; Zhang, Y.; Guo, Y.; Liu, S.; Liu, H.; Wu, H. Flakelike LiCoO₂ with Exposed {010} Facets As a Stable Cathode Material for Highly Reversible Lithium Storage. *ACS Appl. Mater. Interfaces* **2016**, *8*, 2723–2731. [[CrossRef](#)] [[PubMed](#)]
17. Lin, Q.; Sha, Y.; Zhao, B.; Chen, Y.; Tadé, M.O.; Shao, Z. In situ electrochemical creation of cobalt oxide nanosheets with favorable performance as a high tap density anode material for lithium-ion batteries. *Electrochim. Acta* **2015**, *180*, 914–921. [[CrossRef](#)]
18. Porcher, W.; Moreau, P.; Lestriez, B.; Jouanneau, S.; Le Cras, F.; Guyomard, D. Stability of LiFePO₄ in water and consequence on the Li battery behaviour. *Ionics* **2008**, *14*, 583–587. [[CrossRef](#)]
19. Zaghbi, K.; Dontigny, M.; Charest, P.; Labrecque, J.F.; Guerfi, A.; Kopec, M.; Mauger, A.; Gendron, F.; Julien, C.M. Aging of LiFePO₄ upon exposure to H₂O. *J. Power Sources* **2008**, *185*, 698–710. [[CrossRef](#)]
20. Wang, J.; Yang, J.; Tang, Y.; Li, R.; Liang, G.; Sham, T.K.; Sun, X. Surface aging at olivine LiFePO₄: A direct visual observation of iron dissolution and the protection role of nano-carbon coating. *J. Mater. Chem. A* **2013**, *1*, 1579–1586. [[CrossRef](#)]
21. Orlenius, J.; Lyckfeldt, O.; Kasvayee, K.A.; Johander, P. Water based processing of LiFePO₄/C cathode material for Li-ion batteries utilizing freeze granulation. *J. Power Sources* **2012**, *213*, 119–127. [[CrossRef](#)]
22. Guerfi, A.; Kaneko, M.; Petitclerc, M.; Mori, M.; Zaghbi, K. LiFePO₄ water-soluble binder electrode for Li-ion batteries. *J. Power Sources* **2007**, *163*, 1047–1052. [[CrossRef](#)]

23. Hoelzel, M.; Senyshyn, A.; Dolotko, O. SPODI: High resolution powder diffractometer. *JLSRF* **2015**, *1*. [[CrossRef](#)]
24. Degen, T.; Sadki, M.; Bron, E.; König, U.; Nénert, G. The HighScore suite. *Powder Diffraction* **2014**, *29*, S13–S18. [[CrossRef](#)]
25. Thompson, P.; Cox, D.E.; Hastings, J.B. Rietveld refinement of Debye-Scherrer synchrotron X-ray data from Al_2O_3 . *J. Appl. Crystallogr.* **1987**, *20*, 79–83. [[CrossRef](#)]
26. Finger, L.W.; Cox, D.E.; Jephcoat, A.P. A correction for powder diffraction peak asymmetry due to axial divergence. *J. Appl. Crystallogr.* **1994**, *27*, 892–900. [[CrossRef](#)]
27. Pawley, G.S. Unit-cell refinement from powder diffraction scans. *J. Appl. Crystallogr.* **1981**, *14*, 357–361. [[CrossRef](#)]
28. Taylor, R.; Kennard, O. Accuracy of crystal structure error estimates. *Acta Crystallogr. B Struct. Sci.* **1986**, *42*, 112–120. [[CrossRef](#)]
29. Schwarzenbach, D.; Abrahams, S.C.; Flack, H.D.; Gonschorek, W.; Hahn, T.; Huml, K.; Marsh, R.E.; Prince, E.; Robertson, B.E.; Rollett, J.S.; et al. Statistical descriptors in crystallography: Report of the IUCr Subcommittee on Statistical Descriptors. *Acta Crystallogr. A Found. Crystallogr.* **1989**, *45*, 63–75. [[CrossRef](#)]
30. Toby, B.H.R. Factors in Rietveld analysis: How good is good enough? *Powder Diffraction* **2006**, *21*, 67–70. [[CrossRef](#)]
31. Kaduk, J.A.; Partenheimer, W. Chemical accuracy and precision in Rietveld analysis: The crystal structure of cobalt(II) acetate tetrahydrate. *Powder Diffraction* **1997**, *12*, 27–39. [[CrossRef](#)]
32. Yi, T.F.; Hu, X.G.; Dai, C.S.; Gao, K. Effects of different particle sizes on electrochemical performance of spinel LiMn_2O_4 cathode materials. *J. Mater. Sci.* **2007**, *42*, 3825–3830. [[CrossRef](#)]
33. Xu, J.; Deshpande, R.D.; Pan, J.; Cheng, Y.T.; Battaglia, V.S. Electrode side reactions, capacity loss and mechanical degradation in lithium-ion batteries. *J. Electrochem. Soc.* **2015**, *162*, A2026–A2035. [[CrossRef](#)]



© 2017 by the authors. Licensee MDPI, Basel, Switzerland. This article is an open access article distributed under the terms and conditions of the Creative Commons Attribution (CC BY) license (<http://creativecommons.org/licenses/by/4.0/>).